Principles and simulations of high-resolution STM imaging with a flexible tip apex

Ondrej Krejčí,[1,2,*] Prokop Hapala,[1] Martin Ondráček,[1] and Pavel Jelínek[1,3]

[1]*Institute of Physics of the Czech Academy of Sciences, v.v.i., Cukrovarnická 10, 162 00 Prague, Czech Republic*

[2]*Charles University in Prague, Faculty of Mathematics and Physics, Department of Surface and Plasma Science, V Holešovičkách 2, 180 00 Prague, Czech Republic*

[3]*Donostia International Physics Center (DIPC), Paseo Manuel Lardizabal 4, E-20018 San Sebastian, Spain*

We present a robust but still efficient simulation approach for high-resolution scanning tunneling microscopy (STM) with a flexible tip apex showing sharp submolecular features. The approach takes into account the electronic structure of the sample and tip as well as relaxation of the tip apex. We validate our model by achieving good agreement with various experimental images which allows us to explain the origin of several observed features. Namely, we have found that the high-resolution STM mechanism consists of standard STM imaging, convolving electronic states of the sample and the tip apex orbital structure, with the contrast heavily distorted by the relaxation of the flexible apex caused by interaction with the substrate.

I. INTRODUCTION

Both scanning tunneling microscopy (STM) [1] and atomic force microscopy (AFM) [2] have demonstrated the capability to achieve submolecular resolution with a properly functionalized tip apex [3,4]. The unprecedented spatial resolution has advanced the characterization of atomic clusters [5], single molecules [6–8], their assemblies [9,10], and mutual interactions [11,12], as well as the understanding of on-surface chemical reactions [13,14] including the identification of intermediate and final products [15,16].

The origin of submolecular AFM contrast is well established [9,17–19]. In general, the sharp submolecular contrast results from a lateral bending of a flexible tip apex [in our approach represented by a probe particle [18] (PP)]. This bending is caused by a lateral force acting on the tip apex, which results from an interplay between the repulsive Pauli, attractive van der Waals', and electrostatic forces [8]. Sharp edges representing apparent bonds in AFM images [6,20] are the consequence of a discontinuity in the lateral bending of the flexible apex above ridge lines of the potential energy landscape, which are typically located above atoms or bonds [9,18,21].

In principle, high-resolution STM (HR-STM) imaging represents an experimentally less demanding way to achieve submolecular contrast compared to AFM. Furthermore, it provides information about the electronic structure, in addition to the physical structure, of the inspected molecules. Thus, information provided by STM is, in principle, superior to AFM. However, a detailed understanding of the HR-STM imaging mechanism is still missing [18,22,23], impeding its wider proliferation.

Previously, we demonstrated [18,24] that the relaxation of the flexible PP attached to the tip can partially explain the submolecular contrast observed not only in AFM, but also in STM and inelastic electron tunneling spectroscopy (IETS) [25] images . However, the original STM model [18] completely neglects the electronic structure in the description of the tunneling process between tip and sample. The fact that such a crude tunneling model was able to reproduce to some extent the sharp features visible in HR-STM experiments further emphasizes the importance of accounting for the tip apex relaxation in the close-distance regime. On the other hand, numerous HR-STM experiments [1,23,26] indicate that the submolecular contrast depends very much on various experimental details—such as the bias voltage, the substrate, or the microscopic structure of the STM tip apex. Thus, it is evident that the electronic structure has to be included in the correct description of HR-STM imaging.

Traditional STM simulation methods are based on either a nonperturbative approach [27–29] or a perturbative approach (e.g., in Ref. [30]). The latter is only valid when the tip and sample remain out of physical contact [31]. It frequently uses the Bardeen approach [32] and subsequent approximations derived by Chen [33–35] or Tersoff and Hamann [36] (TH). Importantly, the STM methods were devised for surfaces of solid-state materials with a rigid tip apex. Thus they do not take into account any tip apex relaxation, which is fundamental for the understanding of the submolecular contrast with functionalized tips.

In this work, we present an efficient STM model, which takes into account both the PP relaxation as well as electronic wave functions of tip and sample. We will show that this model (hereafter referred to as PP-STM) [37] is able to explain experimentally observed features, which could not be properly reproduced with either the original simple model [18] or traditional STM methods.

II. METHODS

A. Description of the PP-STM model

1. General description of the tunneling process

High-resolution AFM/STM images with functionalized tips are typically acquired at very close distances where repulsive Pauli forces dominate. Therefore, the influence of tip proximity can substantially affect the tunneling barrier [31]. Nevertheless, it has been shown [12] that the tunneling barrier is preserved even in the repulsive regime, due to the presence

---

*Corresponding author: krejcio@fzu.cz

of a low-reactivity functionalized tip apex, such as CO or Xe. Consequently, the perturbative approach describing the tunneling processes still remains valid.

Thus, for a description of the tunneling, we make use of Bardeen tunneling theory [32,34], in which we compose the overall tunneling of contributions from individual eigenstates of the tip T and sample S. Here we write the formula in atomic units ($e = m_e = \hbar = 1$),

$$I = 4\pi \int_0^V \sum_T \sum_S \rho_T(E_F - V + \nu)\rho_S(E_F + \nu)|M_{TS}|^2 d\nu,$$

(1)

where E_F and V are the Fermi level and applied sample bias voltage, respectively; ρ_S and ρ_T stand for the density of states (DOS) of sample and tip, respectively, at the corresponding energy. Finally, M_{TS} represents the tunneling matrix elements between the states T and S [32,34]. In our method, we consider both tip DOS ρ_T and the tunneling matrix elements M_{TS} to be energetically independent. The conductance G at sample bias voltage V can be simply expressed from Eq. (1),

$$G(V) \equiv \frac{dI}{dV}(V) = 4\pi \sum_T \sum_S \rho_T \rho_S(E_F + V)|M_{TS}|^2.$$

(2)

The summations in both Eqs. (1) and (2) go across the eigenstates of tip T and sample S, which are involved in the tunneling process at the given energy, as shown in Fig. 1. Next,
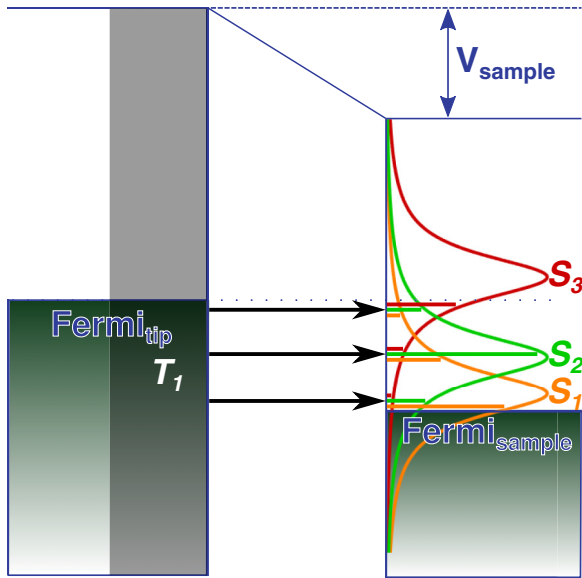

FIG. 1. Schematic illustration of the current calculations: One state of the tip T_1 and three states of sample S_1–S_3 contribute to the current only. The state of the tip T_1 has constant density, while the states of the sample have some Lorentzian broadening around their eigenenergies. The contributions to the tunneling coming from each state of the sample at different energies are illustrated by the full bars on the sample side. The state S_3 contributes to the tunneling, even though the state itself is above the tunneling window. However, its tail gives significant contribution nearby to the upper edge of the tunneling window. In the calculations, the contributions are multiplied by the square of the tunneling matrix elements, $|M_{TS}|^2$.

we will discuss separately the DOS of the sample (ρ_S) and tip (ρ_T), together with tunneling matrix elements M_{TS}.

2. Density of states of tip ρ_T

In our approach, the flexible tip is approximated by the last atom of the relaxing tip apex, which is represented by the PP [18,24]. The positions of the tilting PP are precalculated by a PP-AFM code [18,24], as discussed in Sec. III.

In principle, the DOS ρ_T of the tip apex could be obtained from a density functional theory (DFT) calculation for a given tip model. The DOS of the apex can depend on the atomic and chemical structure of both the flexible frontier atom/molecule and a metallic tip base. But typically the precise structure of the metallic tip base in experiments is unknown.

Therefore, we opt for a different strategy, where the tip electronic structure is described by separate s, p_x, p_y, and p_z orbitals located on the PP. The DOS corresponding to each of these orbitals is assumed to be energetically independent. Each of these PP orbitals provides a separate tunneling channel between the PP and sample. We attribute to each DOS of the PP orbital ρ_T a weight between 0 and 1. This allows us to easily analyze the impact of each PP orbital on the calculated STM images and to find the best agreement with experimental evidence. We should note that in the present version, the orbitals on the PP do not tilt with the relaxing PP.

In the case of a weakly bound tip apex (e.g., a Xe atom), additional tunneling can appear—both between the sample and the PP, as expected, as well as between the PP and tip [18]. Here we consider only the tunneling between the PP and the sample. The validity of this approach is supported by good agreement with experimental evidence, as discussed in Sec. III. However, we cannot rule out that in some cases, the second tunneling can further modulate the calculated signal.

3. Density of states of sample ρ_S

The DOS of the sample ρ_S for given eigenstate S is represented by a Lorentzian function,

$$\rho_S(V; \eta) = \frac{1}{2\pi} \frac{\eta}{(\varepsilon_S - V)^2 + \eta^2},$$

(3)

where ε_S is the eigenenergy of states S, which is obtained from the total-energy DFT calculations of the sample structure. The η is a broadening factor typically ∼0.1 eV.

The total-energy DFT calculations of the sample can be carried out with different codes based on the linear combination of atomic orbitals (LCAO) formalism, for consistency with the formalism in which the tunneling matrix M_{TS} is represented (see discussion later). At the moment, three LCAO DFT codes can be used for creation of input files for the PP-STM code: FIREBALL [38], GPAW [39,40] in LCAO mode [41], and FHI-AIMS [42], but other codes could be easily adapted as well.

4. Tunneling matrix elements M_{TS}

The tunneling matrix elements in our approach are approximated by the Chen rules [33,34]. The matrix elements M_{TS} derived in the LCAO formalism can be composed of

contributions from separate atoms a (of the sample),

$$M_{TS} = \sum_{a \in \text{atoms of sample}} \frac{2\pi}{\kappa} T_{Ta}^{\text{Chen}}, \qquad (4)$$

where the decay constant $\kappa = \sqrt{2W}$ is given by the work function of the sample W [33,34]. The hopping element T_{Ta}^{Chen} represents the contribution from a single atom a derived from the Chen's rules, depending on the corresponding symmetry of the PP orbital T [33,34],

$$T_{Ta}^{\text{Chen}} = \sum_{\alpha \in \text{atom orbitals}} \begin{cases} C_s \phi_\alpha(\vec{r}_a) & \text{if } T \text{ is } s \\ C_p \frac{\partial}{\partial \gamma} \phi_\alpha(\vec{r}_a) & \text{if } T \text{ is } p_\gamma, \end{cases} \qquad (5)$$

where $\gamma \in \{x, y, z\}$ and $\vec{r}_a = \vec{r}_a^{\text{sample}} - \vec{R}^{\text{PP}}$. Vector $\vec{r}_a^{\text{sample}}$ stands for positions of atoms of the sample and $\vec{R}^{\text{PP}}$ is the position of the PP (tip). The constants C_s and C_p are set to $C_s = 1$ and $C_p = \frac{\sqrt{3}}{\kappa}$ according to a derivation shown in Appendix A. We reconstruct the pseudoatom orbital's wave function $\phi_\alpha(\vec{r}_a)$ from the LCAO coefficients of the DFT calculations, standard (real number) spherical harmonics, and a radial part. The radial part is, for simplicity, approximated by a single exponential, given by the characteristic decay length constant κ, which is directly related to the work function of the sample. Here the exponential form ensures the correct decay of the wave function from surface to vacuum [36] and it is assumed to be the same for all atoms of the sample:

$$\phi_\alpha = 2\kappa^{3/2} C_a \exp(-\kappa |\vec{r}_a|) \times \begin{cases} \frac{1}{\sqrt{4\pi}} c_{S,a,s}^{\text{LCAO}} & \text{if } \alpha \text{ is } s \\ \frac{\sqrt{3}}{\sqrt{4\pi}} \frac{y_a}{|\vec{r}_a|} c_{S,a,p_y}^{\text{LCAO}} & \text{if } \alpha \text{ is } p_y \\ \frac{\sqrt{3}}{\sqrt{4\pi}} \frac{z_a}{|\vec{r}_a|} c_{S,a,p_z}^{\text{LCAO}} & \text{if } \alpha \text{ is } p_z \\ \frac{\sqrt{3}}{\sqrt{4\pi}} \frac{x_a}{|\vec{r}_a|} c_{S,a,p_x}^{\text{LCAO}} & \text{if } \alpha \text{ is } p_x, \end{cases}$$
$$(6)$$

where x_a, y_a, and z_a are Cartesian components of the vector $\vec{r}_a$. The constants $c_{S,a,\alpha}^{\text{LCAO}}$ represent LCAO coefficients of the sample's state S, atom a, and atomic orbital α obtained from the DFT calculations. Since the PP-STM code is made for the calculation of current (or conductivity) flowing from/to adsorbed organic molecules, we consider for simplicity only the valence s and p sample atom orbitals as orbitals α in this work. But the extension of the PP-STM methods including d and f electrons can be done in a straightforward manner.

Finally, we introduced a constant C_a in Eq. (6) in order to have the possibility of changing the amplitude of the atomic tunneling hoppings T_{Ta}^{Chen}. Therefore, we refer to it as the amplitude constant. We typically assume the same amplitude constant ($C_a = 1$) for all atoms of the sample. This approximation of the hoppings gives us good agreement with experiments for two systems—the perylenetetracarboxylic dyanhydride (PTCDA) molecule adsorbed on Au(111) and Ag(111) (see Sec. III A and III B). However, in the case of strongly polarized 1,5,9-trioxo-13-azatriangulene (TOAT) adsorbed on Cu(111), the amplitude of the exponential can be modified by a variation of a tunneling barrier above different atoms of the sample. We discuss this in detail in Sec. III C.

The examples of the fully expanded atomic hoppings T_{Ta}^{Chen} and the matrix elements M_{TS} are shown in Appendix B.

B. Details of DFT calculations

1. PTCDA/Au(111)

We based a slab representing experimentally observed herringbone reconstruction of PTCDA molecules on Au(111) [Fig. 2(a)] on the geometry described by Martínez *et al.* [43]. The Au(111) slab was composed of three layers with Au lattice constant 4.18 and 30 Å of vacuum above it. The topmost golden layer together with the molecular layer were optimized by means of VASP DFT code [44]. For the optimization of the geometry, a GGA-PW91 functional [45], ultrasoft pseudopotentials [46], and Grimme description of van der Waals interactions [47] were applied. The energy cutoff of 396 eV was used for the plane-wave basis set. The force criterion for the differences of the total energy between the optimization steps was set to 10^{-5} eV.

The calculation of the LCAO coefficients was performed with FIREBALL [38] code, using the local density approximation (LDA) functional calculated on a grid with energy cutoff of 300 eV. The Brillouin zone was represented by a Γ point only. The valence basis set and radial cuts for the localized orbitals are shown in Table I of Appendix C. In order to better describe the states of the substrate with Γ point, a 2×2 supercell was used for these calculations [shown in Fig. 3(a)]. The DOS projected on the PTCDA molecules is shown in Fig. 3(b).

2. PTCDA/Ag(111)

The geometry of experimentally observed herringbone reconstruction of PTCDA/Ag(111) [Figs. 4(a) and 4(b)] was constructed according to Rohlfing *et al.* [48]. The Ag(111) slab was comprised of three nonrelaxed layers of Ag, with lattice constant 4.09 Å. 30 Å of vacuum above the slab was used in the three-dimensional (3D) periodic boundary conditions. The molecular layer located 3 Å above the substrate was not relaxed.

The LCAO coefficients were also calculated with the FIREBALL code and the same parameters (2×2 supercell with Γ point and basis in Table I in Appendix C) as described above for the PTCDA/Au(111). The supercell together with the DOS projected on the molecules are shown in Figs. 3(c) and 3(d), respectively. The Hartree potential used for the PP-AFM calculations was also computed by the FIREBALL code.

3. TOAT/Cu(111)

For DFT calculations of the TOAT molecule on Cu(111), we make use of a geometry obtained with cluster calculations in Ref. [49] that describes the most often observed configuration of the molecule on the surface. The almost flat molecule sits 3.3 Å above the copper layer with oxygens being placed 0.15 Å closer to the substrate [49]. The original small Cu cluster under the molecule was expanded to 91 Cu atoms [shown in Fig. 5(a)] to provide a better description of the substrate. This bigger cluster was used for the calculations of the LCAO coefficients to describe a molecule adsorbed far from other molecules. These

calculations were performed with the GPAW code [39–41] in order to show that different codes could be adapted for the PP-STM calculations. The calculations were done with the LDA functional in the LCAO mode and the default basis set. The DOS projected only on the molecule from the GPAW is shown in Fig. 5(b).

The Hartree potential, used for the PP-AFM calculations and for the study of the element-dependent tunneling barrier discussed in Sec. III C, was taken from the original DFT calculations [49]. The shape of the Hartree potential above different atoms of the adsorbed TOAT molecule is shown in Fig. 5(c).

C. PP-AFM calculations

The PP-AFM simulations were done with the PP model described in [18,24]. The calculation of the Lennard-Jones (LJ) force field were done with default LJ parameters [18] (taken from the optimized potential for liquid simulations (OPLS) force field [50]). For these calculations, only the topmost atoms—atoms of the adsorbed molecules—contributed to the LJ force field. The Xe atom on the tip apex was represented by the PP with Xe LJ parameters, while the CO molecule was represented only by oxygen LJ parameters. If the tip apex is charged, the charge Q is represented by a Gaussian cloud with its FWHM of 0.71 Å located on the PP [24]. The PP is positioned 4 Å below the last metal tip atom. The height scale used in the following text denotes the height of the PP above the molecule before relaxation. After the relaxation, the PP can become up to 0.14 Å higher, especially at very close distance scans, where the PP relaxes a lot. This height scale differs from that in Refs. [8,18,24,49].

1. PTCDA/Au(111)

The PP position calculations of PTCDA/Au(111) were done with the default spring stiffness K of 0.5 N/m. In these calculations, no electrostatics were used. The PP was placed 3.2 Å above the molecule for the PTCDA/Au(111) close-distance scan simulations.

2. PTCDA/Ag(111)

The PP-AFM computations were done with the PP parameters that were fitted in Ref. [8] for the set obtained with a positively charged Xe tip: spring stiffness $K = 0.2$ N/m and charge $Q = 0.3$ elementary charge (e). The far- and close-distance scans were calculated with the PP being placed 4.3 and 3.7 Å above the molecule, respectively.

3. TOAT/Cu(111)

The spring stiffness K and the charge Q were set according to the findings in Ref. [8] in the PP-AFM calculations. Namely, they were $K = 0.24$ N/m, $Q = +0.3$ e for the Xe tip simulations, and $K = 0.24$ N/m, $Q = 0.0$ e for the CO tip simulations. For the far-distance Xe tip scan, we positioned the PP 4.9 Å above the molecule, while for the close-distance scan, we positioned the PP 3.5 Å above the molecule. The close-distance scan obtained with the CO tip was simulated with the PP being placed 2.9 Å above the molecule.

III. RESULTS AND DISCUSSION

In what follows, we will examine our approach by comparison with experimental HR-STM images obtained above three different systems: PTCDA molecule adsorbed on Au(111) [43,51] and Ag(111) [8,48] surfaces and TOAT molecule adsorbed on Cu(111) surfaces [49]. The experimental measurements were done in a constant-height STM mode with very low applied bias voltage or in a constant-height dI/dV mode. Since the experimental images acquired with very low bias voltage can be seen as dI/dV maps, all simulated STM images were calculated as constant-height dI/dV maps at a particular energy.

A. PTCDA/Au(111)

Figure 2(a) shows the experimental dI/dV map of PTCDA/Au(111) acquired with a CO-terminated tip at the energy corresponding to the highest occupied molecular orbital (HOMO) of PTCDA [51]. The molecular skeleton is rendered by the characteristic sharp edges, with a pronounced depression of the dI/dV signal located in the central part of the molecule. To disentangle the effect of the electronic structure and the PP relaxation, we first calculated a dI/dV map at the energy of the HOMO without the PP relaxation at a close tip-sample distance; see Fig. 2(b). The combination of the HOMO orbital [shown in the inset of Fig. 2(b)] with p_x and p_y orbitals on the fixed PP transforms the original 12 lobes of the orbital into five stripes at each side of the molecule and four squares in the middle of it. It is noteworthy that unlike the TH, our approach takes into account the cancellation of an STM signal, due to interference effects [35,52,53], that plays an important role in the formation of the STM signal. For example, the destructive interference takes place in the middle of the molecule, where the different phases of the sample and tip orbitals lead to a cancellation of the calculated signal. However, the calculated STM image with fixed PP [Fig. 2(b)] lacks sharp edges and overall agreement with the experimental counterpart is poor.

In the next step, we perform STM simulations including the PP relaxation with the same tip-sample distance and energy; see Fig. 2(c). The impact of the PP relaxation is substantial and the resulting STM image agrees very well with the experimental evidence; compare Fig. 2(a) with 2(c). Namely, the PP relaxations distort the smooth signal giving rise to the sharp edges above the potential ridges. The effect of the relaxation is more clearly pronounced on a comparison of line profiles taken above the center of the molecule; see Fig. 2(d). When the PP is located above a central hexagon, it relaxes towards its center to minimize the interaction energy [positions of the PP are shown in Fig. 2(e)]. Therefore, the signal taken above the central hexagon is almost constant. The sharp edges are also visible on the image obtained with an s orbital on the relaxing PP [Fig. 2(f)]; however, this simulation does not match well with the experimental image. Conversely, the very good agreement between the image simulated with p_x and p_y orbitals on the PP [Fig. 2(c)] and the experimental image obtained with a CO tip in the dI/dV mode [Fig. 2(a)] indicates that the electronic structure of the
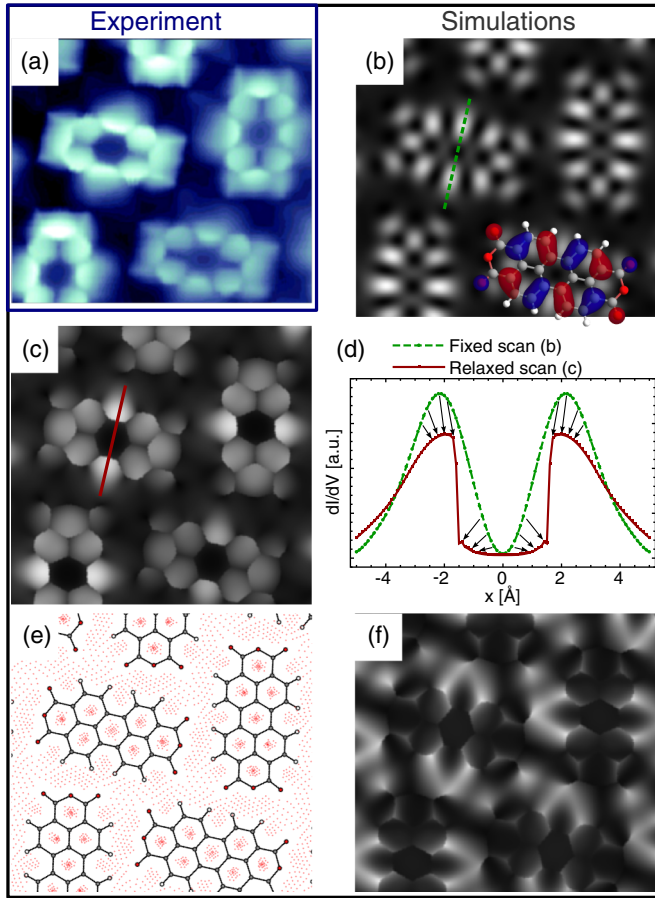
FIG. 2. Comparison between experimental and theoretical STM images calculated with rigid and flexible tip apex. (a) Experimental constant-height HR-STM dI/dV figure of PTCDA/Au(111) obtained with CO tip at $V_{bias} = -1.6$ V with respect to the sample [51]. (b),(c) Constant-height dI/dV simulations of PTCDA/Au(111) at the energy of HOMO of PTCDA obtained via our PP-STM code using p_x and p_y orbitals on the probe particle (PP) originally placed 3.2 Å above the molecule, with the (b) fixed and (c) relaxed PP, respectively. (d) Comparison of line profiles, taken above centers of PTCDA molecules as indicated by (b) the green dashed line for fixed PP and (c) the red full line for relaxed PP. The arrows indicate the changes in the dI/dV signal given by the PP relaxations. (e) Positions of the relaxed PP, indicated by red dots, when (c) and (f) were simulated. (f) The same scan as (c), but with s orbital on the PP. PP parameters: $K = 0.5$ N/m. All dI/dV scans are done above the area of 25×25 Å.

CO tip in this experiment can be well described with p_x and p_y orbitals.

The appearance of sharp edges and the main part of the STM (dI/dV) contrast depends on the PP deviations, and the k stiffness is almost arbitrary—for lower stiffnesses, the deviations appear at higher z positions of tip, and the other way around. Since our main purpose was to show the general mechanism of the HR-STM imaging, we did not try to estimate the stiffness from the comparison with various PP-STM simulations proceeded with different lateral stiffnesses.

It is noteworthy that the PP-STM represents a very efficient method, as the calculated STM images shown in Fig. 2(c),
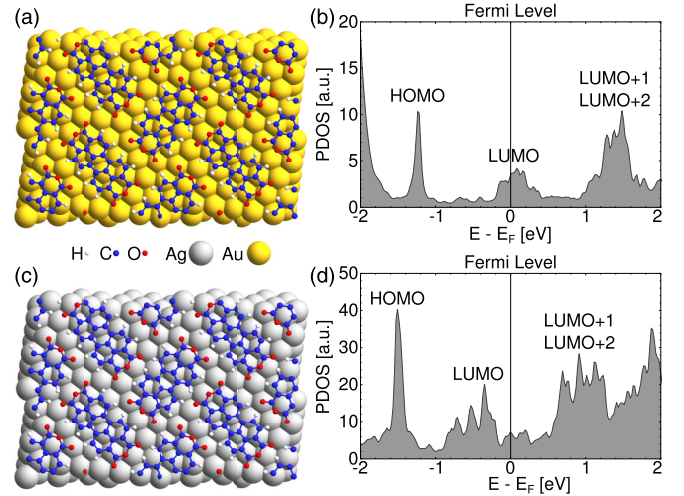

FIG. 3. Properties of PTCDA on Au(111) and Ag(111) surface. (a) Geometry of PTCDA molecules adsorbed on a Au(111) surface. (b) Density of states projected on the molecules for the PTCDA/Au(111) system. (c) Geometry of PTCDA molecules adsorbed on Ag(111) surface. (d) Density of states projected on the molecules for the PTCDA/Ag(111) system. The shown 2×2 supercells in (a) and (c) were used for calculations of the LCAO coefficients. The colors of the atoms are shown in the inset between (a) and (c).

including about 1200 atoms, take only 1 hour on a standard workstation computer.

B. PTCDA/Ag(111)

Figures 4(a) and 4(b) display experimental images of PTCDA molecules adsorbed on an Ag(111) surface obtained with a Xe tip at low sample bias voltage ($V_{bias} = -2$ mV [8]) in two different tip-sample distances. Figure 4(a) was acquired in a far tip-sample distance, when tip apex relaxation is not expected. The second experimental image [Fig. 4(b)] was obtained at a smaller tip-sample distance, when the sharp edges in both AFM and STM channels begin to appear. More importantly, the Xe tip in this experimental session was found to be positively charged [8].

Figures 4(c) and 4(d) show calculated STM images obtained with the positively charged Xe tip model ($Q = +0.3 \ e$) [8], where we considered only an s orbital on the PP. The good agreement between the experimental STM images [Figs. 4(a) and 4(b)] and their theoretical counterparts [Figs. 4(c) and 4(d)] validates our approach for both far and close tip-sample distances. While in the far-distance regime, the STM contrast is exclusively driven by the electronic structure of both tip and sample, in the close-distance regime the distinctive sharp edges [Figs. 4(b) and 4(d)] coincide with the edges in the HR-AFM image [8]. The positive charge located on the tip apex diminishes the apparent size of the anhydride groups at the edge of the PTCDA molecules in both STM and AFM [8]. This observation confirms that HR-STM images can potentially also be used for an analysis of the electrostatic field [8].

In this case, we were not able to reproduce the experimental contrast considering only freestanding molecule states. That is in contrast to the PTCDA/Au(111) system, where the
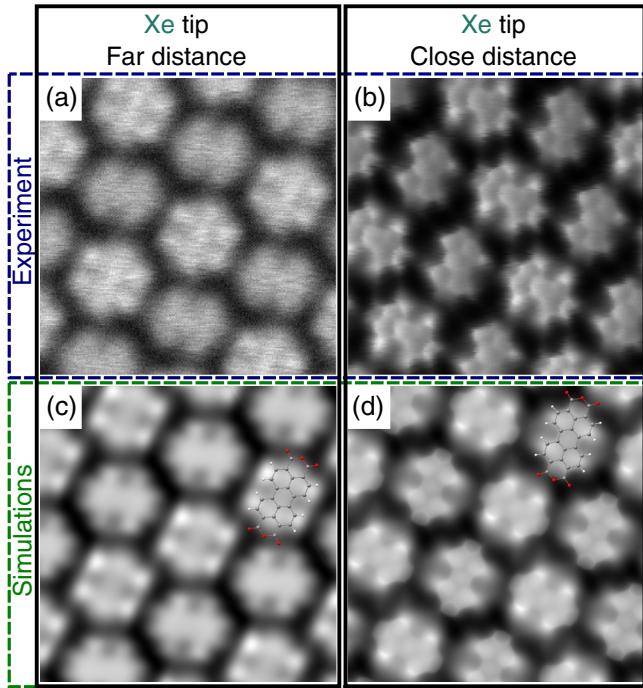
FIG. 4. Comparison of the PP-STM model with experiment—PTCDA/Ag(111)—for different heights of the tip. (a),(b) Constant-height HR-STM obtained with Xe tip and $V_{bias} = -2$ mV in (a) far and (b) close tip-sample distances, respectively. (c),(d) Simulated PP-STM (dI/dV) images with s orbital on the PP, which is placed (c) 4.3 Å and (d) 3.7 Å above the molecule. The simulation energy is $+0.1$ eV above the Fermi level. PP parameters: $Q = +0.3\,e$ and $K = 0.2$ N/m. All figures show area 39×39 Å.
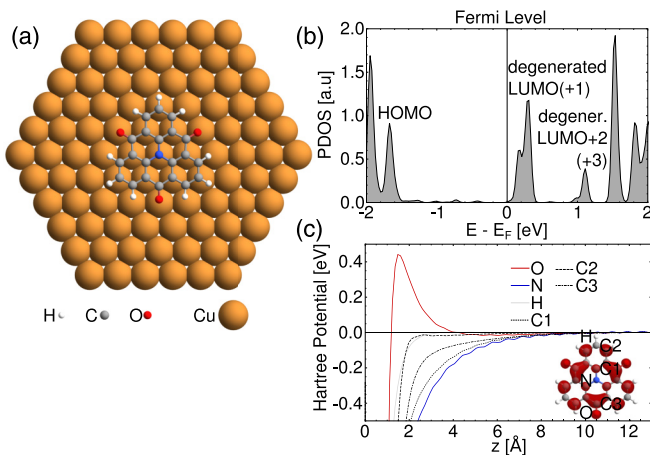

FIG. 5. Properties of TOAT molecule on Cu(111) surface. (a) Geometry of a single molecule adsorbed on a Cu(111) surface. Cluster calculations were used to describe an isolated molecule on the surface. (b) Density of states projected on the molecule for the TOAT/Cu(111) system. (c) Hartree potential profiles taken above the atoms of the molecule. The selected atoms are depicted in the inset, in the right bottom corner. The Hartree potential was taken from original calculations in Ref. [49].

molecular HOMO state was intrinsic to the STM signal. Here the role of the Ag substrate is very important. The simulated images were obtained at energy -0.1 eV below the Fermi level, where the interface states originating from hybridization of the lowest unoccupied molecular orbital (LUMO) with the metallic substrate are located; see Fig. 3(b).

C. TOAT/Cu(111)

In the last example, we will demonstrate not only that other molecules can be simulated, but also that the contrast difference between Xe and CO functionalized tips can be captured by our simulations. We will examine STM images of TOAT molecules deposited on Cu(111) surfaces, which has a large internal charge transfer due to the presence of an N atom in the center and three O atoms on the periphery of the molecule [8]. Figures 6(a) and 6(b) show STM images obtained with a Xe tip in the far- and close-distance regimes, while Fig. 6(c) was acquired with a CO tip in the close-distance regime [49]. We see that the STM contrast obtained in the close-distance regime with Xe and CO tips is quite different.
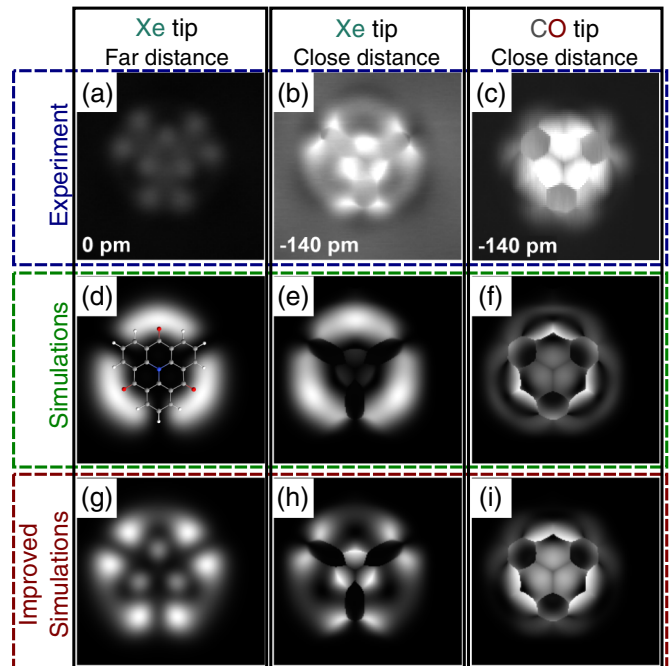

FIG. 6. Comparison of the PP-STM model with experiment—TOAT/Cu(111)—for different tips and heights. (a)–(c) Experimental constant-height HR-STM images of a single TOAT molecule adsorbed on Cu(111) [49], obtained with Xe tip at $V_{bias} = 200$ mV in (a) large tip-sample distance and (b) tip-sample distance lowered by 1.40 Å. (c) A HR-STM image obtained with a CO tip with small tip-sample distance at $V_{bias} = 100$ mV. (d),(e) PP-STM simulations at energy $+0.2$ eV above the Fermi level, with s orbital on the PP ($K = 0.24$ N/m; $Q = +0.3\,e$) for PP height (d) 4.9 Å and (e) 3.5 Å above the molecule. (f) PP-STM simulation at energy $+0.2$ eV above the Fermi level, with p_x and p_y orbitals on the PP ($K = 0.24$ N/m; $Q = 0.0\,e$) at height 2.9 Å above the molecule. (g)–(i) The same PP-STM simulations as (d) and (f), but with C_a constant for oxygen on the sample lowered by a factor of two. The area of all shown figures is 19×19 Å.

The impact of the functionalized tips is twofold. First, an additive electrostatic interaction between PP and the strong electric field of the molecule may significantly change the PP relaxation and, consequently, the apparent position of sharp edges [8]. In the previous work [8], we estimated, from the detailed comparison of the experimental and simulated AFM images, an effective charge for Xe and CO to be $+0.3\,e$ and $0.0\,e$, respectively. Second, the different electronic wave functions of the functional group on a probe may change the STM contrast. In the next analysis, we will describe the wave function of Xe and CO tips by s and p_x, p_y orbitals on the PP, respectively, as they already provided the very good matches in the previous cases of PTCDA molecules.

Figures 6(d) and 6(e) represent calculated STM images for a positively charged Xe tip, while Fig. 6(f) shows a simulated STM image using a neutral CO tip, both at energy +0.2 eV above the Fermi level. The effect of different effective charge can be nicely seen from a different apparent shape of outer benzene rings in the close-distance images [Figs. 6(b) and 6(c)]. Different orbital symmetries of the tip wave function give rise to distinct contrast in the STM images (compare, e.g., different contrast in the central part and on periphery of the molecule). However, overall agreement between the experiment and the simulation is not very good, especially on the periphery of the molecule.

One possible explanation can be related to the more complex electronic structure of the probe. In particular, Gross *et al.* [52] achieved good agreement between STM images acquired with CO tips in the far-distance regime by taking into account the linear combination of s, p_x, and p_y orbitals on the probe. Pavlíček *et al.* [54] claimed that the p and s contributions can depend on the applied bias voltage. However, in our case, the combinations of $s - p$ orbitals do not improve the agreement with the experimental data.

On the other hand, from analysis of the Hartree potential above the adsorbed molecule, we found a local increase of the tunneling barrier above the oxygens due to a negative partial charge on the oxygen [see Fig. 5(c)]. We tried to mimic the variation of the tunneling barrier by lowering the C_a constant for the oxygen atoms by a factor of two. The HR-STM simulations displayed in Figs. 6(g)–6(i) show significant improvements in the match with the experimental figures for both tip functionalizations and for both tip-sample distance regimes.

More rigorous treatment of the C_a constant, by taking into consideration the local variation of the potential barrier height, is left as a subject for further development. Alternatively, the atomic hoppings T_{Ta} from Eq. (5) could be calculated numerically according to a procedure described in Ref. [29]. We would like to emphasize that many other parameters (e.g., chemical and atomic structure of the whole tip apex including metallic base, charges induced due to the applied bias voltage and/or tip-sample proximity [12], and tunneling between the PP and the tip [18]), which are not taken into account in our model, could also play a role in varying the STM contrast. Despite this fact, we found the PP-STM model provides satisfactory agreement with the available experimental data.

IV. CONCLUSION

In conclusion, we have introduced the PP-STM model for simulations of HR-STM images acquired with a flexible tip apex. The PP-STM model takes into account both the relaxation of the probe particle and the tunneling process between electronic states of the sample and the tip. We have employed the Bardeen theory to describe the tunneling process, while the relaxation of the probe particle is described by the mechanistic PP-AFM model [18,24]. We have performed extensive comparison of simulated HR-STM images with experimental evidence to demonstrate the validity and the limits of the PP-STM model. The model sheds more light on the HR-STM mechanism, which consists of the standard STM imaging heavily distorted by the relaxation of the flexible tip apex. We believe that the detailed understanding of the high-resolution mechanism of STM imaging will serve the further proliferation of application of this technique.

APPENDIX A: DERIVATION OF THE C_s AND C_p CONSTANTS

The constants C_s and C_p are not the Chen's constants C_{lm} that in the original paper describe the tip state composed of many atomic orbitals [33]. In our approach, the states of the tip are single atomic orbitals. The constants C_s and C_p are introduced to the PP-STM model to have mirror symmetry between the tip and the sample: For the same atom on the PP and on the sample, it is natural to expect that the tunneling between the s orbital on the tip and the p_z orbital on the sample would give the same contributions as the contribution obtained with the switched orbitals. This can be rewritten as

$$T_{sa}^{\text{Chen}} = T_{p_z a}^{\text{Chen}}, \qquad (A1)$$

where, for the left hopping, $c_{S,a,s}^{\text{LCAO}} = c_{S,a,p_y}^{\text{LCAO}} = c_{S,a,p_x}^{\text{LCAO}} = 0$ and $c_{S,a,p_z}^{\text{LCAO}} = 1$, and for the right hopping, $c_{S,a,p_z}^{\text{LCAO}} = c_{S,a,p_y}^{\text{LCAO}} = c_{S,a,p_x}^{\text{LCAO}} = 0$ and $c_{S,a,s}^{\text{LCAO}} = 1$. Now the left hopping can be rewritten according to Eq. (B1) without its zero contributions,

$$T_{sp_z}^{\text{Chen}} = 2\kappa^{3/2} C_s C_a \exp(-\kappa|\vec{r}_a|) \frac{1}{\sqrt{4\pi}} \left[\sqrt{3}\frac{z_a}{|\vec{r}_a|} \right]. \qquad (A2)$$

An analogy to Eq. (B2) for the p_z orbital on the tip can be derived from Eqs. (5) and (6). Here we show only the

part without the zero contribution necessary for the constants derivation,

$$T_{p_z s}^{\text{Chen}} = 2\kappa^{3/2} C_p C_a \exp(-\kappa|\vec{r}_a|) \frac{1}{\sqrt{4\pi}} \frac{1}{|\vec{r}_a|} [z_a \kappa]. \quad \text{(A3)}$$

Since we do not require quantitative agreement with experiment and since C_s is arbitrary in the previous consideration, we set it to one ($C_s = 1$). Now, the constant C_p can be enumerated from Eqs. (A2) and (A3),

$$C_p = \frac{\sqrt{3}}{\kappa}. \quad \text{(A4)}$$

APPENDIX B: EXPANSION OF TUNNELING MATRIX ELEMENTS M_{TS} AND ATOMIC CONTRIBUTIONS T_{Ta}^{Chen}

1. Expansion of atomic contributions T_{Ta}^{Chen}

According to Eq. (5), the atomic hoppings T_{Ta}^{Chen} depend on the symmetry of the tip—more precisely on the orbital T localized on the PP. Here we show two examples of fully expanded T_{Ta}^{Chen} hoppings derived from Eqs. (5) and (6) for s and p_y orbital on the PP:

$$T_{sa}^{\text{Chen}} = 2\kappa^{3/2} C_s C_a \exp(-\kappa|\vec{r}_a|) \frac{1}{\sqrt{4\pi}} \left[c_{S,a,s}^{\text{LCAO}} + \sqrt{3}\frac{y_a}{|\vec{r}_a|} c_{S,a,p_y}^{\text{LCAO}} \right.$$
$$\left. + \sqrt{3}\frac{z_a}{|\vec{r}_a|} c_{S,a,p_z}^{\text{LCAO}} + \sqrt{3}\frac{x_a}{|\vec{r}_a|} c_{S,a,p_x}^{\text{LCAO}} \right] \quad \text{(B1)}$$

and

$$T_{p_y a}^{\text{Chen}} = 2\kappa^{3/2} C_p C_a \exp(-\kappa|\vec{r}_a|) \frac{1}{\sqrt{4\pi}} \frac{1}{|\vec{r}_a|} \left[y_a \kappa c_{S,a,s}^{\text{LCAO}} \right.$$
$$+ \sqrt{3}\left(\frac{y_a^2}{|\vec{r}_a|^2} + \frac{y_a^2}{|\vec{r}_a|}\kappa - 1 \right) c_{S,a,p_y}^{\text{LCAO}}$$
$$+ \sqrt{3}\left(\frac{y_a z_a}{|\vec{r}_a|^2} + \frac{y_a z_a}{|\vec{r}_a|}\kappa \right) c_{S,a,p_z}^{\text{LCAO}}$$
$$\left. + \sqrt{3}\left(\frac{y_a x_a}{|\vec{r}_a|^2} + \frac{y_a x_a}{|\vec{r}_a|}\kappa \right) c_{S,a,p_x}^{\text{LCAO}} \right], \quad \text{(B2)}$$

respectively.

2. Full expansion of M_{sS} for s orbital on PP

$$M_{sS} = \sum_a \sqrt{4\pi\kappa} C_a C_s \exp(-\kappa|\vec{r}_a|) \left[c_{S,a,s}^{\text{LCAO}} + \sqrt{3}\frac{y_a}{|\vec{r}_a|} c_{S,a,p_y}^{\text{LCAO}} \right.$$
$$\left. + \sqrt{3}\frac{z_a}{|\vec{r}_a|} c_{S,a,p_z}^{\text{LCAO}} + \sqrt{3}\frac{x_a}{|\vec{r}_a|} c_{S,a,p_x}^{\text{LCAO}} \right]. \quad \text{(B3)}$$

3. Full expansion of $M_{p_y S}$ for p_y orbital on PP

$$M_{p_y S} = \sum_a \sqrt{4\pi\kappa} C_a C_p \exp(-\kappa|\vec{r}_a|) \frac{1}{|\vec{r}_a|} \left[y_a \kappa c_{S,a,s}^{\text{LCAO}} \right.$$
$$+ \sqrt{3}\left(\frac{y_a^2}{|\vec{r}_a|^2} + \frac{y_a^2}{|\vec{r}_a|}\kappa - 1 \right) c_{S,a,p_y}^{\text{LCAO}}$$
$$+ \sqrt{3}\left(\frac{y_a z_a}{|\vec{r}_a|^2} + \frac{y_a z_a}{|\vec{r}_a|}\kappa \right) c_{S,a,p_z}^{\text{LCAO}}$$
$$\left. + \sqrt{3}\left(\frac{y_a x_a}{|\vec{r}_a|^2} + \frac{y_a x_a}{|\vec{r}_a|}\kappa \right) c_{S,a,p_x}^{\text{LCAO}} \right]. \quad \text{(B4)}$$

APPENDIX C: TABLE OF RADIAL CUTS FOR FIREBALL BASIS SET

The radial cut off radii of numerical basis set used in the PP-STM simulations are listed in Table I.

TABLE I. The radial cuts for the basis set used in the FIREBALL calculations. a_b stands for the Bohr radius. * marks an excited orbital.

Atom	Orbital	Radial cut (a_b)	Atom	Orbital	Radial cut (a_b)
H	s	4.0	Ag	s	4.5
	$s*$	4.0		p	5.5
				$s*$	4.0
C	s	4.5	Au	s	4.5
	p	4.5		p	5.6
	d	5.4		d	4.3
O	s	3.3			
	p	3.8			
	$s*$	3.3			
	$p*$	3.8			

[1] R. Temirov, S. Soubatch, O. Neucheva, A. C. Lassise, and F. S. Tautz, New J. Phys. **10**, 053012 (2008).

[2] L. Gross, F. Mohn, N. Moll, P. Liljeroth, and G. Meyer, Science **325**, 1110 (2009).

[3] L. Bartels, G. Meyer, K.-H. Rieder, D. Velic, E. Knoesel, A. Hotzel, M. Wolf, and G. Ertl, Phys. Rev. Lett. **80**, 2004 (1998).

[4] F. Mohn, B. Schuler, L. Gross, and G. Meyer, Appl. Phys. Lett. **102**, 073109 (2013).

[5] M. Emmrich, F. Huber, F. Pielmeier, J. Welker, M. Schneiderbauer, T. Hofmann, D. Meuer, S. Polesya, S. Mankovsky, D. Kodderitzsch, H. Ebert, and F. J. Giessibl, Science **348**, 308 (2015).

[6] L. Gross, F. Mohn, N. Moll, B. Schuler, A. Criado, E. Guitián, D. Peña, A. Gourdon, and G. Meyer, Science **337**, 1326 (2012).

[7] F. Albrecht, J. Repp, M. Fleischmann, M. Scheer, M. Ondráček, and P. Jelínek, Phys. Rev. Lett. **115**, 076101 (2015).

[8] P. Hapala, M. Svec, O. Stetsovych, N. J. van der Heijden, M. Ondracek, J. van der Lit, P. Mutombo, I. Swart, and P. Jelínek, Nat. Commun. **7**, 11560 (2016).

[9] S. K. Hämäläinen, N. van der Heijden, J. van der Lit, S. den Hartog, P. Liljeroth, and I. Swart, Phys. Rev. Lett. **113**, 186102 (2014).

[10] S. Kawai, A. Sadeghi, X. Feng, P. Lifen, R. Pawlak, T. Glatzel, A. Willand, A. Orita, J. Otera, S. Goedecker, and E. Meyer, ACS Nano **7**, 9098 (2013).

[11] Z. Sun, M. Boneschanscher, I. Swart, D. Vanmaekelbergh, and P. Liljeroth, Phys. Rev. Lett. **106**, 046104 (2011).

[12] M. Corso, M. Ondracek, C. Lotze, P. Hapala, K. J. Franke, P. Jelinek, and J. I. Pascual, Phys. Rev. Lett. **115**, 136101 (2015).

[13] L. Gross, N. Moll, G. Meyer, R. Ebel, W. M. Abdel-Mageed, and M. Jaspars, Nat. Chem. **2**, 821 (2010).

[14] N. Pavliček, B. Schuler, S. Collazos, N. Moll, D. Pérez, E. Guitián, G. Meyer, D. Peña, and L. Gross, Nat. Chem. **7**, 623 (2015).

[15] D. G. de Oteyza, P. Gorman, Y.-C. Chen, S. Wickenburg, A. Riss, D. J. Mowbray, G. Etkin, Z. Pedramrazi, H.-Z. Tsai, A. Rubio, M. F. Crommie, and F. R. Fischer, Science **340**, 1434 (2013).

[16] B. Schuler, G. Meyer, D. Peña, O. C. Mullins, and L. Gross, J. Am. Chem. Soc. **137**, 9870 (2015).

[17] N. Moll, L. Gross, F. Mohn, A. Curioni, and G. Meyer, New J. Phys. **12**, 125020 (2010).

[18] P. Hapala, G. Kichin, C. Wagner, F. S. Tautz, R. Temirov, and P. Jelínek, Phys. Rev. B **90**, 085421 (2014).

[19] C.-S. Guo, M. A. Van Hove, X. Ren, and Y. Zhao, J. Phys. Chem. C **119**, 1483 (2015).

[20] N. Pavliček, C. Herranz-Lancho, B. Fleury, M. Neu, J. Niedenführ, M. Ruben, and J. Repp, Phys. Status Solidi B **250**, 2424 (2013).

[21] M. P. Boneschanscher, S. K. Hämäläinen, P. Liljeroth, and I. Swart, ACS Nano **8**, 3006 (2014).

[22] J. I. Martínez, E. Abad, C. González, F. Flores, and J. Ortega, Phys. Rev. Lett. **108**, 246102 (2012).

[23] C. Weiss, C. Wagner, C. Kleimann, M. Rohlfing, F. S. Tautz, and R. Temirov, Phys. Rev. Lett. **105**, 086103 (2010).

[24] P. Hapala, R. Temirov, F. S. Tautz, and P. Jelínek, Phys. Rev. Lett. **113**, 226101 (2014).

[25] C. l. Chiang, C. Xu, Z. Han, and W. Ho, Science **344**, 885 (2014).

[26] P. Hapala, M. Ondráček, O. Stetsovych, M. Švec, and P. Jelínek, *Noncontact Atomic Force Microscopy: Vol. 3* (Springer International, Cham, Switzerland, 2015), pp. 29–49.

[27] J. Cerdá, M. A. Van Hove, P. Sautet, and M. Salmeron, Phys. Rev. B **56**, 15885 (1997).

[28] N. Mingo, L. Jurczyszyn, F. J. Garcia-Vidal, R. Saiz-Pardo, P. L. de Andres, F. Flores, S. Y. Wu, and W. More, Phy. Rev. B **54**, 2225 (1996).

[29] J. M. Blanco, F. Flores, and R. Pérez, Prog. Surf. Sci. **81**, 403 (2006).

[30] W. Hofer, Prog. Surf. Sci. **71**, 147 (2003).

[31] J. M. Blanco, C. Gonzalez, P. Jelinek, J. Ortega, F. Flores, and R. Perez, Phys. Rev. B **70**, 085405 (2004).

[32] J. Bardeen, Phys. Rev. Lett. **6**, 57 (1961).

[33] C. J. Chen, Phys. Rev. B **42**, 8841 (1990).

[34] C. J. Chen, *Introduction to Scanning Tunneling Microscopy*, Vol. 2 (Oxford University Press, New York, 2008).

[35] G. Mándi and K. Palotás, Phys. Rev. B **91**, 165406 (2015).

[36] J. Tersoff and D. R. Hamann, Phys. Rev. B **31**, 805 (1985).

[37] https://github.com/ProkopHapala/ProbeParticleModel/tree/PPSTM (unpublished).

[38] J. P. Lewis, P. Jelínek, J. Ortega, A. A. Demkov, D. G. Trabada, B. Haycock, H. Wang, G. Adams, J. K. Tomfohr, E. Abad, H. Wang, and D. A. Drabold, Phys. Status Solidi B **248**, 1989 (2011).

[39] J. J. Mortensen, L. B. Hansen, and K. W. Jacobsen, Phys. Rev. B **71**, 035109 (2005).

[40] J. Enkovaara *et al.*, J. Phys.: Condens. Matter **22**, 253202 (2010).

[41] A. H. Larsen, M. Vanin, J. J. Mortensen, K. S. Thygesen, and K. W. Jacobsen, Phys. Rev. B **80**, 195112 (2009).

[42] V. Blum, R. Gehrke, F. Hanke, P. Havu, V. Havu, X. Ren, K. Reuter, and M. Scheffler, Comput. Phys. Commun. **180**, 2175 (2009).

[43] J. Martínez, E. Abad, F. Flores, J. Ortega, and G. Brocks, Chem. Phys. **390**, 14 (2011).

[44] G. Kresse and J. Furthmüller, Phys. Rev. B **54**, 11169 (1996).

[45] J. P. Perdew, J. A. Chevary, S. H. Vosko, K. A. Jackson, M. R. Pederson, D. J. Singh, and C. Fiolhais, Phys. Rev. B **46**, 6671 (1992).

[46] D. Vanderbilt, Phys. Rev. B **41**, 7892 (1990).

[47] S. Grimme, J. Comput. Chem. **27**, 1787 (2006).

[48] M. Rohlfing, R. Temirov, and F. S. Tautz, Phys. Rev. B **76**, 115421 (2007).

[49] N. J. van der Heijden, P. Hapala, J. A. Rombouts, J. van der Lit, D. Smith, P. Mutombo, M. Švec, P. Jelínek, and I. Swart, ACS Nano **10**, 8517 (2016).

[50] W. L. Jorgensen and J. Tirado-Rives, J. Am. Chem. Soc. **110**, 1657 (1988).

[51] G. Kichin, C. Wagner, F. S. Tautz, and R. Temirov, Phys. Rev. B **87**, 081408 (2013).

[52] L. Gross, N. Moll, F. Mohn, A. Curioni, G. Meyer, F. Hanke, and M. Persson, Phys. Rev. Lett. **107**, 086101 (2011).

[53] M. Telychko, P. Mutombo, M. Ondráček, P. Hapala, F. C. Bocquet, J. Kolorenč, M. Vondráček, P. Jelínek, and M. Švec, ACS Nano **8**, 7318 (2014).

[54] N. Pavliček, I. Swart, J. Niedenführ, G. Meyer, and J. Repp, Phys. Rev. Lett. **110**, 136101 (2013).